Inorg. Chem. **2009**, *48*, 4421−4434

Facile Synthesis and Unique Physicochemical Properties of Three-Dimensionally Ordered Macroporous Magnesium Oxide, Gamma-Alumina, and Ceria−Zirconia Solid Solutions with Crystalline Mesoporous Walls

Huining Li, Lei Zhang, Hongxing Dai,* and Hong He

Laboratory of Catalysis Chemistry and Nanoscience, Department of Chemistry and Chemical Engineering, College of Environmental and Energy Engineering, Beijing University of Technology, Beijing 100124, China

Received January 21, 2009

Three-dimensionally (3D) ordered macroporous (3DOM) MgO, γ-Al_2O_3, $Ce_{0.6}Zr_{0.4}O_2$, and $Ce_{0.7}Zr_{0.3}O_2$ with polycrystalline mesoporous walls have been successfully fabricated with the triblock copolymer $EO_{106}PO_{70}EO_{106}$ (Pluronic F127) and regularly packed monodispersive polymethyl methacrylate (PMMA) microspheres as the template and magnesium, aluminum, cerium and zirconium nitrate(s), or aluminum isopropoxide as the metal source. The as-synthesized metal oxides were characterized by means of techniques such as X-ray diffraction (XRD), thermogravimetric analysis/differential scanning calorimetry (TGA/DSC), Fourier transform infrared (FT-IR), high-resolution scanning electron microscopy (HRSEM), high-resolution transmission electron microscopy/selected area electron diffraction (HRTEM/SAED), BET, carbon dioxide temperature-programmed desorption (CO_2-TPD), and hydrogen temperature-programmed reduction (H_2-TPR). It is shown that the as-fabricated MgO, γ-Al_2O_3, $Ce_{0.6}Zr_{0.4}O_2$, and $Ce_{0.7}Zr_{0.3}O_2$ samples possessed single-phase polycrystalline structures and displayed a 3DOM architecture; the MgO, $Ce_{0.6}Zr_{0.4}O_2$, and $Ce_{0.7}Zr_{0.3}O_2$ samples exhibited worm-hole-like mesoporous walls, whereas the γ-Al_2O_3 samples exhibited 3D ordered mesoporous walls. The solvent (ethanol or water) nature and concentration, metal precursor, surfactant, and drying condition have an important impact on the pore structure and surface area of the final product. The introduction of surfactant F127 to the synthesis system could significantly enhance the surface areas of the 3DOM metal oxides. With PMMA and F127 in a 40% ethanol solution, one can generate well-arrayed 3DOM MgO with a surface area of 243 m^2/g and 3DOM $Ce_{0.6}Zr_{0.4}O_2$ with a surface area of 100 m^2/g; with PMMA and F127 in an ethanol−HNO_3 solution, one can obtain 3DOM γ-$Al_2O_3$with a surface area of 145 m^2/g. The 3DOM MgO and 3DOM γ-Al_2O_3 samples showed excellent CO_2 adsorption behaviors, whereas the 3DOM $Ce_{0.6}Zr_{0.4}O_2$ sample exhibited exceptional low-temperature reducibility. The unique physicochemical properties associated with the copresence of 3DOM and mesoporous walls make these porous materials ideal candidates for applications in heterogeneous catalysis and CO_2 adsorption.

1. Introduction

Meso- or macroporous materials possess high surface areas, two-dimensional (2D) or three-dimensional (3D) porous architecture, and large pore volumes. These unique characteristics make them ideal for potential application in the physical and chemical fields. Among the nonsiliceous porous materials, magnesium oxide, activated alumina (γ-Al_2O_3), and ceria−zirconia ($Ce_{1-x}Zr_xO_2$) solid solutions with abundant 2D or 3D pore structure are very important.

Up to now, most porous materials synthesized are either acidic or neutral.[1−3] There are rare reports on the generation

* To whom correspondence should be addressed. Phone: +86-10-6739-6588. Fax: +86-10-6739-6588. E-mail: hxdai@bjut.edu.cn.

(1) Tsuji, H.; Yagi, F.; Hattori, H. *Chem. Lett.* **1991**, *1*, 1881.
(2) Wang, Y.; Zhu, J. H.; Cao, J. M.; Chun, Y.; Xu, Q. H. *Microporous Mesoporous Mater.* **1998**, *26*, 175.
(3) Yu, J. I.; Shiau, S. Y.; Ko, A. N. *Catal. Lett.* **2001**, *77*, 165.

10.1021/ic900132k CCC: $40.75
Published on Web 04/06/2009

of basic porous materials. It is known that alkalinity is a crucial factor influencing the catalytic or adsorptive behavior of a material. Hence, it is highly desired to develop an alternative strategy to make porous materials with intrinsic basicity. MgO is a useful solid base catalyst[4,5] or catalyst support.[6,7] The MgO usually prepared using conventional methods (e.g., the decomposition of various magnesium salts and $Mg(OH)_2$[8]) possesses a relatively low surface area and small micropores, thus limiting its wide application. Such a disadvantage can be avoided if mesoporous MgO with high surface area, large pore volume, and narrow pore-size distribution is synthesized.[9,10] In recent years, a number of mesoporous MgO materials with ordered mesoporosity are prepared via the surfactant-assisted sol−gel route[11] or through the nanocasting (with mesoporous silica or carbon materials as the hard template) process.[9,10,12]

Alumina is an important material for applications in ultrafiltration of salts,[13] as an adsorbent in environmental cleanup,[14] as an automobile exhaust catalyst,[15] as a heterogeneous catalyst support for hydrodechlorination,[16] and in petroleum refinement.[17] Porous γ-alumina with uniform channels, high surface area, and narrow pore-size distribution possesses even better physicochemical properties. However, the fabrication of ordered and thermally stable porous alumina is complicated[18] due to its susceptibility for hydrolysis and phase transition-induced destruction of ordered pore structure. Therefore, disordered structures with amorphous walls are usually obtained in most cases.[19−24] For example, by strictly controlling the hydrolysis and condensation processes, Somorjai et al.[25] fabricated ordered mesoporous alumina with amorphous walls. The hydrolysis behavior of alumina has been reported to be strongly influenced by acid, water, temperature, relative humidity, and other factors.[25−28] With aluminum tri-*tert*-butoxide as the main Al source and $AlCl_3$ as the pH adjustor and hydrolysis−condensation controller, Tian et al. generated partly ordered mesoporous Al_2O_3.[29] Recently, several research groups have prepared mesostructured γ-alumina with crystalline framework.[29−34] For instance, by utilizing the dip-coating strategy, Sanchez et al. synthesized ordered γ-alumina nanocrystalline films with a mesoporous architecture.[32] With the aid of aerosol generation of the initial solution with an TSI (Trust, Science, Innovation; model 3076) as the atomizer, Boissière et al. fabricated ordered mesoporous gamma-alumina nanocrystallites that were stable up to 900 °C.[33] Through a nanocasting (with CMK-3 as the hard template) process, Liu et al.[34] obtained ordered mesoporous crystalline alumina. By adopting a sol−gel process with nonionic block copolymer (Pluronic P123 or F127) as the template in ethanol solvent, Yan and co-workers[35] generated highly ordered 2D hexagonal mesoporous alumina with high thermal stability and tunable pore sizes.

Ceria-based materials have recently attracted much attention because they are commercially employed as the components of ultraviolet radiation absorbers, automotive three-way catalysts (TWCs), solid oxide fuel cells, and glass-polishing materials. The incorporation of zirconia to the ceria lattice can significantly improve the thermal stability, surface area, and reducibility of the TWCs.[36,37] $Ce_{1-x}Zr_xO_2$ solid solutions in an ordered porous structure with crystalline walls are expected to show enhanced catalytic performance due to their large surface area and a certain degree of size- and shape-selectivity. Since the fabrication of cubic mesostructured CeO_2-ZrO_2 thin films,[38] a number of publications on the synthesis and catalytic applications of mesoporous $Ce_{1-x}Zr_xO_2$ appeared in the literature.[39,40] Recently, highly ordered 2D mesoporous $Ce_{1-x}Zr_xO_2$ solid solutions with crystalline walls have been reported by Yan and co-workers who adopted a sol−gel process combined with evaporation-

(4) Llamas, R.; Ruiz, J. R. *Appl. Catal., A* **2007**, *72*, 18.
(5) Climent, M. J.; Corma, A.; Iborra, S.; Primo, J. *J. Catal.* **1995**, *151*, 60.
(6) Aceves, B. A.; Novaro, O.; López, T.; Gómez, R. *J. Phys. Chem.* **1995**, *99*, 14403.
(7) Crisafulli, C.; Maggiore, R.; Sciré, S.; Solarino, L.; Galvagno, S. *J. Mol. Catal.* **1990**, *63*, 55.
(8) Ranjit, K. T.; Klabunde, K. J. *Chem. Mater.* **2005**, *17*, 65.
(9) Roggenbuck, J.; Tiemann, M. *J. Am. Chem. Soc.* **2005**, *127*, 1096.
(10) Roggenbuck, J.; Koch, G.; Tiemann, M. *Chem. Mater.* **2006**, *18*, 4151.
(11) Wang, G.; Zhang, L.; Dai, H.; Deng, J.; Liu, C.; He, H.; Au, C. T. *Inorg. Chem.* **2008**, *47*, 4015.
(12) Li, J.; Dai, W.-L.; Fan, K. *J. Phys. Chem. C* **2008**, *112*, 17657.
(13) Schaep, J.; Vandecasteele, C.; Peeters, B.; Luyten, J.; Dotremont, C.; Roels, D. *J. Membr. Sci.* **1999**, *163*, 229.
(14) Kim, Y.; Kim, C.; Choi, I.; Rengaraj, S.; Yi, J. *Environ. Sci. Technol.* **2004**, *38*, 924.
(15) Narula, C. K.; Allison, J. E.; Bauer, D. B.; Gandhi, H. S. *Chem. Mater.* **1996**, *8*, 984.
(16) Kim, P.; Kim, Y.; Kim, C.; Kim, H.; Park, Y.; Lee, J. H.; Song, I. K.; Yi, J. *Catal. Lett.* **2003**, *89*, 185.
(17) Zhang, Z.; Hicks, R. W.; Pauly, T. R.; Pinnavaia, T. J. *J. Am. Chem. Soc.* **2001**, *123*, 1592.
(18) Čejka, J. *Appl. Catal., A* **2003**, *254*, 327.
(19) Bagshaw, S. A.; Prouzet, E.; Pinnavaia, T. J. *Science* **1995**, *269*, 1242.
(20) Vaudry, F.; Khodabandeh, S.; Davis, M. E. *Chem. Mater.* **1996**, *8*, 1451.
(21) Yada, M.; Ohya, M.; Machida, M.; Kijima, T. *Chem. Commun.* **1998**, 1941.
(22) Cabrera, S.; Haskouri, J. E.; Alamo, J.; Beltrán, A.; Betrán, D.; Mendioroz, S.; Marcos, M. D.; Amorós, P. *Adv. Mater.* **1999**, *11*, 379.
(23) Bagshaw, S. A.; Pinnavaia, T. J. *Angew. Chem., Int. Ed.* **1996**, *35*, 1102.
(24) Zhang, W.; Pinnavaia, T. J. *Chem. Commun.* **1998**, 1185.
(25) Niesz, K.; Yang, P.; Somorjai, G. A. *Chem. Commun.* **2005**, 1986.
(26) Baes, C. F; Mesmer, R. E. *The Hydrolysis of Cations*; Wiley: New York, 1976; p 112.
(27) Swaddle, T. W.; Rosenqvist, J.; Yu, P.; Bylaska, E.; Phillips, B. L.; Casey, W. H. *Science* **2005**, *308*, 1450.
(28) Casey, W. H. *Chem. Rev.* **2006**, *106*, 1.
(29) Tian, B. Z.; Yang, H. F.; Liu, X. Y.; Xie, S. H.; Yu, C. Z.; Fan, J.; Tu, B.; Zhao, D. Y. *Chem. Commun.* **2002**, 1824.
(30) Zhang, Z. R.; Hicks, R. W.; Pauly, T. R.; Pinnavaia, T. J. *J. Am. Chem. Soc.* **2002**, *124*, 1592.
(31) Zhang, Z. R.; Pinnavaia, T. J. *J. Am. Chem. Soc.* **2002**, *124*, 12294.
(32) Kuemmel, M.; Grosso, D.; Boissière, C.; Smarsly, B.; Brezesinski, T.; Albouy, P. A.; Amenitsch, H.; Sanchez, C. *Angew. Chem., Int. Ed.* **2005**, *44*, 4589.
(33) Boissière, C.; Nicole, L.; Gervais, C.; Babonneau, F.; Antonietti, M.; Amenitsch, H.; Sanchez, C.; Grosso, D. *Chem. Mater.* **2006**, *18*, 5238.
(34) Liu, Q.; Wang, A. Q.; Wang, X. D.; Zhang, T. *Chem. Mater.* **2006**, *18*, 5153.
(35) Yuan, Q.; Yin, A.-X.; Luo, C.; Sun, L.-D.; Zhang, Y.-W.; Duan, W.-T.; Liu, H.-C.; Yan, C.-H. *J. Am. Chem. Soc.* **2008**, *130*, 3465.
(36) Kašpar, J.; Fornasiero, P.; Graziani, M. *Catal. Today* **1999**, *50*, 285.
(37) Kašpar, J.; Fornasiero, P.; Hickey, N. *Catal. Today* **2003**, *77*, 419.
(38) Crepaldi, E. L.; Soler-Illia, G. J. D. A.; Bouchara, A.; Grosso, D.; Durand, D.; Sanchez, C. *Angew. Chem., Int. Ed.* **2003**, *42*, 347.
(39) Brezesinski, T.; Antonietti, M.; Groenewolt, M.; Pinna, N.; Smarsly, B. *New J. Chem.* **2005**, *29*, 237.
(40) Huo, C.; Yu, J. C.; Wang, X.; Lai, S.; Qiu, Y. *J. Mater. Chem.* **2005**, *15*, 2193.

induced self-assembly in ethanol using P123 as the template and ceric nitrate and zirconium oxychloride as the metal source without additional acid or base.[41]

In recent years, much attention has been focused on three-dimensionally ordered macroporous (3DOM) materials with pore size in the submicrometer scale due to their applications in photonic crystals, catalysis, and separation.[42−44] The most commonly adopted method for obtaining 3DOM metal oxides is an alkoxide-based sol−gel process using a colloidal crystal (i.e., ordered monodispersive micospheres, such as polystyrene (PS), poly(methyl methacrylate) (PMMA), silica, or carbon) as the hard template and liquid metal alkoxides, nitrates, or acetates as the metal source, followed by calcination or extraction for template removal. The as-generated interconnected macropore materials with high porosity facilitate transport of guest molecules and particles in potential catalysis and filtration. An alternative strategy for producing 3DOM metal oxides was reported by Yan et al.[45] They infiltrated metal acetates or nitrates into voids of the well-arrayed colloidal crystal microspheres and solidified them as the corresponding oxalates via the interaction of the incorporated metal salts and oxalic acid in the voids, thus giving rise to 3DOM-structured MgO and other transition oxides after subsequent thermal treatments. With PMMA as the hard template, aluminum nitrate as the Al source, and ammonium hydroxide as the precipitating agent, Sokolov et al. obtained 3DOM alpha-alumina (<24 m^2/g) after high-temperature calcination.[46] By using an ethylene glycol (EG) and methanol mixed solution of metal nitrate salts, Ueda and co-workers reported the generation of well-aligned 3DOM mixed oxides $La_{1-x}Sr_xFeO_{3-\delta}$ ($x = 0-0.4$) and MFe_2O_4 (M = Zn, Ni, Co).[47−49] On the basis of the above method, the same group proposed an improved approach to fabricate 3DOM alumina, iron oxide, chromium oxide, manganese oxide, and their mixed-metal oxides.[50] They observed that the efficient removal of heat released due to oxidative decomposition of PMMA was important to produce well-ordered 3DOM materials effectively.

Although 3DOM materials can be synthesized according to the above-mentioned methods, their surface areas are still relatively low and the pores are only macropores without mesopore formation on the walls. These drawbacks inhibit wide application of such porous materials. Therefore, high-surface-area 3DOM materials with mesopore walls are highly desirable. Although silica with a bimodal distribution of meso- and macropores[51−53] or micro- and macropores[54] can be fabricated, metal oxides with hierarchically meso- and macroporous structures are rarely seen in the literature. Recently, we used P123 as the soft template, regularly packed PMMA microspheres as the hard template, and tetraethyl orthosilicate as the Si source to successfully make 3DOM silica with 2D ordered mesoporous walls and an unusually large pore volume (2.1 cm^3/g). Following this idea, we introduced P123 or F127 to the mixed PMMA−metal precursor alcoholic solution and fabricated a number of 3DOM metal oxides with mesoporous walls. In this work, we report the facile synthesis, characterization, and physicochemical properties of high-surface-area 3DOM MgO, γ-Al_2O_3, and $Ce_{1-x}Zr_xO_2$ ($x = 0.3$, 0.4) with crystalline mesoporous walls.

2. Experimental Section

2.1. Synthesis of Highly Ordered PMMA Colloidal Crystal Microspheres. The PMMA colloidal crystal microspheres were synthesized using a slightly modified emulsifier-free emulsion polymerization approach.[55] In a typical synthesis, a three-necked round-bottomed alaskite reactor (1000 mL) filled with 650 mL of deionized water equipped with a magnetic stirrer was heated by a hot water bath. A water-cooling condenser with the upper end connected to a wash-bottle containing 30% ethanol (to prevent back-diffusion of air to the reaction system) was fixed to the reactor. In order to remove the air in the reactor, a pipet for pure N_2 introduction was also connected to the vessel. Under constant stirring (350 rpm) and with N_2 bubbling, the water was kept at 70 °C for 30 min and then 55 mL of methyl methacrylate monomer inhibited with ca. 0.03% *p*-hydroxyl benzoic acid was poured into the reactor through the third opening which was otherwise closed with a stopper. After further stirring and N_2 bubbling at 70 °C for 15 min, a solution of potassium persulfate initiator (0.20 g dissolved in 20 mL of deionized water) preheated to 70 °C was added. With N_2 bubbling and stirring, the reaction was allowed to run at 70 °C for 40 min, and the resulting emulsion was diluted with 2000 mL of deionized water and stored up at room temperature. The PMMA colloidal crystal microspheres were left suspended in the liquid medium. By centrifugation of the PMMA-containing liquid at 1000 rpm for 12 h, the clear liquid was decanted and the solid block was dried in centrifugal tubes at ambient temperature, thus obtaining the highly ordered PMMA arrays. The PMMA colloidal crystal microspheres are ca. 298 nm in average diameter (Figure S1 of the Supporting Information).

2.2. Fabrication of 3DOM MgO with Worm-hole-like Mesoporous Walls. The single-phase MgO samples with 3DOM structures and mesoporous walls were prepared as follows: 1.0 g of Pluronic F127 ($EO_{106}PO_{70}EO_{106}$) was dissolved in 10.0 g of ethanol aqueous solution (20−95 wt %), and then, 0.01 mol of magnesium nitrate hexahydrate and 0.01 mol of citric acid were added under stirring; after dissolution, 5.0 g of highly ordered PMMA colloidal

(41) Yuan, Q.; Liu, Q.; Song, W.-G.; Feng, W.; Pu, W.-L.; Sun, L.-D.; Zhang, Y.-W.; Yan, C.-H. *J. Am. Chem. Soc.* **2007**, *129*, 6698.
(42) Schroden, R. C.; Stein, A. In *3D Ordered Macroporous Material, Colloids and Colloid Assemblies*; Caruso, F., Ed.; Wiley-VCH Verlag GmbH and Co. KGaA: Weinheim, Germany, 2004, p 465.
(43) Stein, A.; Schroden, R. C. *Curr. Opin. Solid State Mater. Sci.* **2001**, *5*, 553.
(44) Stein, A. *Microporous Mesoporous Mater.* **2001**, *44−45*, 227.
(45) Yan, H.; Blanford, C. F.; Holland, B. T.; Smyrl, W. H.; Stein, A. *Chem. Mater.* **2000**, *12*, 1134.
(46) Sokolov, S.; Bell, D.; Stein, A. *J. Am. Ceram. Soc.* **2003**, *86*, 1481.
(47) Sadakane, M.; Takahashi, C.; Kato, N.; Ogihara, H.; Nodasaka, Y.; Doi, Y.; Hinatsu, Y.; Ueda, W. *Bull. Chem. Soc. Jpn.* **2007**, *80*, 677.
(48) Sadakane, M.; Takahashi, C.; Kato, N.; Asanuma, T.; Ogihara, H.; Ueda, W. *Chem. Lett.* **2006**, *35*, 480.
(49) Sadakane, M.; Asanuma, T.; Kubo, J.; Ueda, W. *Chem. Mater.* **2005**, *17*, 3546.
(50) Sadakane, M.; Horiuchi, T.; Kato, N.; Takahashi, C.; Ueda, W. *Chem. Mater.* **2007**, *19*, 5779.
(51) Yang, P.; Deng, T.; Zhao, D.; Feng, P.; Pine, D.; Chmelka, B. F.; Whitesides, G. M.; Stucky, G. D. *Science* **1998**, *282*, 2244.
(52) Luo, Q.; Li, L.; Yang, B.; Zhao, D. *Chem. Lett.* **2000**, *29*, 378.
(53) Yang, Z.; Qi, K.; Rong, J.; Wang, L.; Liu, Z.; Yang, Y. *Chin. Sci. Bull.* **2001**, *46*, 1349.
(54) Holland, B. T.; Abrams, L.; Stein, A. *J. Am. Chem. Soc.* **1999**, *121*, 4308.
(55) Zou, D.; Ma, S.; Guan, R.; Park, M.; Sun, L.; Aklonis, J. J.; Salovey, R. *J. Polym. Sci., Part A: Polym. Chem.* **1992**, *30*, 137.

crystal microspheres was added and soaked by the solution. After the PMMA microspheres were thoroughly wetted with the ethanol solution, the excessive liquid was filtered via a Buchner funnel connected to vacuum. Then the sample was dried in a desiccator using anhydrous calcium chloride as desiccating agent (relative humidity < 40%) for 48 h. Finally, the PMMA colloidal crystal microspheres coated with $Mg(NO_3)_2$ were in turn calcined at a heating rate of 1 °C/min from room temperature (RT) to 300 and 550 °C and maintained at the two temperatures for 3 and 5 h, respectively.

2.3. Fabrication of Hierarchically 3DOM Macroporous Gamma-Alumina with Ordered Mesoporous Walls. Hierarchically 3D ordered macro- and mesoporous gamma-alumina was generated as follows: (I) With aluminum nitrate as the Al source, 1.0 g of F127 was first dissolved in a 95 wt % ethanol solution (i.e., 12.0 mL absolute ethanol + 0.5 mL deionized water), and then, 10.0 mmol of $Al(NO_3)_3 \cdot 9H_2O$ was added under stirring. After dissolution, 5.0 g of well-arrayed PMMA colloidal crystal microspheres was added and soaked by the mixed solution. After the PMMA microspheres were wetted thoroughly, the excessive liquid was filtered via the above Buchner funnel and the sample was dried for 48 h under ambient conditions. The aluminum nitrate-coated PMMA microspheres were in turn calcined at a ramp of 1 °C/min from RT to 300 and 600 °C and maintained at those temperatures for 3 and 5 h, respectively. (II) With aluminum isopropoxide ($Al(O^iPr)_3$) as the Al source, (i) 1.0 g of F127 was first dissolved in a 95 wt % ethanol solution (i.e., 6.0 mL absolute ethanol + 0.25 mL deionized water), the obtained mixed solution was called solution A; (ii) 1.2 mL concentrated nitric acid (65−68 wt %) or 1.45 mL concentrated hydrochloric acid (36−38 wt %) was added to 6.0 mL absolute ethanol, after stirring for 15 min, 2.04 g of $Al(O^iPr)_3$ was added gradually to the above inorganic acid−ethanol solution until the Al precursor was completely dissolved, and the obtained mixed solution was called solution B; (iii) under continuously stirring, solution B was gradually poured into solution A and the obtained mixed solution was called solution C; and (iv) 5.0 g of well-arrayed PMMA colloidal crystal microspheres was added and soaked by solution C. The subsequent filtration, drying, and calcination treatments were the same as those described in I.

2.4. Fabrication of 3DOM $Ce_{1-x}Zr_xO_2$ (x = 0.3, 0.4) Solid Solutions with Worm-hole-like Mesoporous Walls. The single-phase $Ce_{1-x}Zr_xO_2$ solid solutions with 3DOM architecture and worm-hole-like mesoporous walls were prepared as follows: 1.0 g of F127 was dissolved in 15.0 g of ethanol aqueous solution (0−95 wt %), and then, in total, 10.0 mmol of stoichiometric $Ce(NO_3)_3 \cdot 6H_2O$ and $ZrO(NO_3)_2 \cdot 2H_2O$ was added under stirring. After complete dissolution, 5.0 g of well-arrayed PMMA colloidal crystal microspheres was added and soaked by the mixed solution. The excessive liquid was filtered via a Buchner funnel connected to vacuum. After being dried for 48 h in the above-mentioned desiccator, the sample was in turn calcined in air at a ramp of 1 °C/min from RT to 300 and 550 °C and kept at these temperatures for 3 and 6 h, respectively.

2.5. Characterization of the As-Fabricated PMMA, MgO, γ-Al_2O_3, and $Ce_{1-x}Zr_xO_2$. Powder X-ray diffraction (XRD) patterns of MgO, γ-Al_2O_3, $Ce_{0.6}Zr_{0.4}O_2$, and $Ce_{0.7}Zr_{0.3}O_2$ samples were recorded on a Bruker/AXS D8 Advance diffractometer operated at 40 kV and 200 mA using Cu Kα radiation and a Ni filter (λ = 0.15406 nm). Crystal phases were identified by referring the diffraction lines to those of the powder diffraction files−1998 ICDD PDF Database. Surface areas, pore size distributions, and N_2 adsorption−desorption isotherms of the samples were measured via N_2 adsorption at −196 °C on an ASAP 2020 (Micromeritics) adsorption analyzer with the samples being outgassed at 250 °C for 2 h under vacuum prior to measurements; surface areas and pore size distributions were calculated according to the Brunauer−Emmett−Teller (BET) and Barrett−Joyner−Halenda (BJH) method, respectively. The high-resolution scanning electron microscopy (HRSEM) images and energy-dispersive X-ray spectroscopy (EDXS) spectra of the samples were recorded by means of an apparatus (Gemini Zeiss Supra 55 and JSM-6490LV) operating at 10 or 20 kV. Before being transferred into the HRSEM chamber, the sample ultrasound-dispersed in ethanol was allowed to settle and dry on a holder before being introduced to a vacuum evaporator for gold deposition. By means of a JEOL-2010 instrument (operated at 200 kV), high-resolution transmission electron microscopy (HRTEM) images and selected area electron diffraction (SAED) patterns of the samples were obtained. Thermogravimetric analysis (TGA) and differential scanning calorimetric (DSC) analysis were conducted in an air flow of 100 mL/min at a ramping rate of 10 °C/min on a SDT Q600 instrument (TA). Fourier transform infrared (FT-IR) spectra (700−4000 cm^{-1} with a resolution of 0.4 cm^{-1}) of the samples (1 wt % sample + 99 wt % KBr) were obtained on a Bruker Vertex 70 spectrometer.

2.6. CO_2 Adsorption Measurement. In order to evaluate the CO_2 adsorption behaviors of the synthesized 3DOM MgO and γ-Al_2O_3 samples, we conducted CO_2 temperature-programmed desorption (CO_2-TPD). The sample was placed in a quartz microreactor (i.d. = 8 mm), and the outlet gases were analyzed online by a Micromeritics Autochem II 2920 instrument. Before the TPD experiment, 50 mg of the as-fabricated sample was thermally treated in helium (flow rate = 30 mL/min) at 550 °C for 1 h, followed by cooling in helium to RT (for the removal of adsorbed water). Then, the sample was exposed to a CO_2 (99.99% in purity) flow of 40 mL/min at RT for 1 h, followed by removal of physisorbed CO_2 by means of helium flushing (He flow = 40 mL/min) at RT for 3 h. The desorption of chemisorbed CO_2 took place in the helium flow with the sample being heated from RT to 840 °C at a rate of 10 °C/min. The amount of CO_2 desorbed from the sample was quantified by calibrating the peak area against that of a standard CO_2 pulse (0.5464 mL).

2.7. Reducibility Evaluation. In order to examine the reducibility of the as-fabricated 3DOM $Ce_{1-x}Zr_xO_2$ solid solutions, we performed the hydrogen temperature-programmed reduction (H_2-TPR) experiments on the Micromeritics Autochem II 2920 instrument. Before measurements, the sample (50 mg) was pretreated in a mixture (20% O_2−80% N_2 (v/v), flow rate = 40 mL/min) at 500 °C for 1 h in a quartz fixed-bed microreactor (i.d. = 6 mm). After cooling to RT in the same atmosphere, the sample was exposed to a flow (50 mL/min) of 10% H_2−90% Ar (v/v) and heated from RT to 800 °C at a ramp of 10 °C/min. The outlet gases were analyzed online by a thermal conductive detector (TCD). The TCD responses were calibrated against that of the complete reduction of a known standard CuO powdered sample (Aldrich, 99.995%).

3. Results and Discussion

3.1. Crystal Structure. The wide-angle and representative small-angle XRD patterns of the as-fabricated MgO, γ-Al_2O_3, $Ce_{0.6}Zr_{0.4}O_2$, and $Ce_{0.7}Zr_{0.3}O_2$ samples are shown in Figure 1A−D. From Figure 1A, one can observe that the positions of XRD lines for all the samples were the same and could be well indexed, as indicated in Figure 1A.a. By comparing the standard MgO XRD pattern (JCPDS PDF no. 78-0430), we deduce that the as-fabricated MgO samples possessed a face-centered cubic crystal structure. Similar results have also

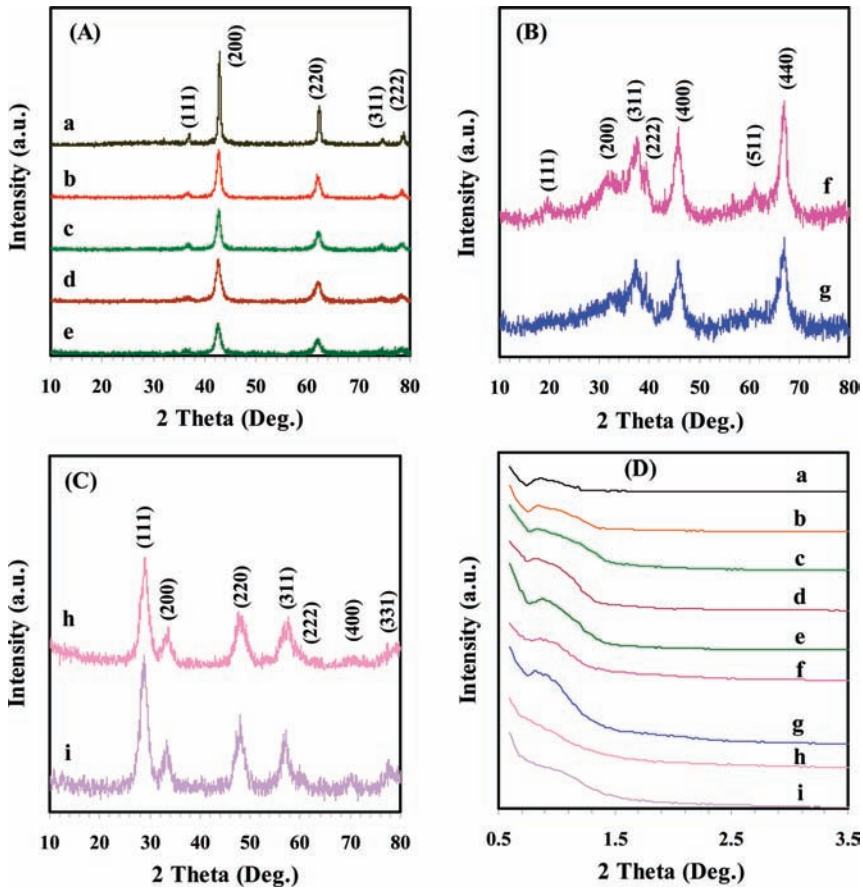

Figure 1. Wide-angle XRD patterns of (A) MgO obtained with (a) PMMA in 95% ethanol solution, (b) PMMA and F127 in aqueous solution, (c) PMMA and F127 in 20% ethanol solution, (d) PMMA and F127 in 40% ethanol solution, and (e) PMMA and F127 in 95% ethanol solution; (B) Al_2O_3 obtained with PMMA and F127 as the template and (f) aluminum nitrate as the Al source in 95% ethanol solution and (g) $Al(O^iPr)_3$ as the Al source in 95% ethanol−HNO_3 solution; (C) $Ce_{0.6}Zr_{0.4}O_2$ (h) and $Ce_{0.7}Zr_{0.3}O_2$ (i) obtained with PMMA and F127 in 40% ethanol solution; and (D) small-angle XRD patterns of the representative MgO, Al_2O_3, $Ce_{0.6}Zr_{0.4}O_2$, and $Ce_{0.7}Zr_{0.3}O_2$ samples.

been reported by other authors who investigated the synthesis and characterization of crystalline mesoporous MgO.[10,56] The intensity of the XRD lines for the five MgO samples was different, with the sample obtained with PMMA in 95% ethanol solution showing the highest in XRD line intensity. The difference in crystallinity of the final products seems to be due to a solvent effect. From Figure 1B, one can see that the wide-angle XRD patterns of the two as-fabricated Al_2O_3 samples were rather similar to that of standard gamma-alumina (JCPDS PDF no. 10-0425), indicating the formation of well-crystallized single-phase face-centered cubic gamma-alumina; the XRD peaks could be well indexed as shown in Figure 1B.f. Furthermore, the crystallinity of the alumina sample synthesized with PMMA and F127 as the template and $Al(NO_3)_3$ as the Al source in 95% ethanol solution was better that that of its counterpart fabricated with PMMA and F127 as the template and $Al(O^iPr)_3$ as the Al source in a 95% ethanol−HNO_3 solution. As seen in Figure 1C, the two ceria−zirconia samples displayed similar XRD patterns with a fluorite-type crystal structure (JCPDS PDF no. 38-1439 for $Ce_{0.6}Zr_{0.4}O_2$ and JCPDS PDF no. 28-0271 for $Ce_{0.75}Zr_{0.25}O_2$), and all the XRD peaks could be indexed as indicated in Figure 1C.h; these results suggest the generation of single-phase cubic crystalline $Ce_{0.6}Zr_{0.4}O_2$ and $Ce_{0.7}Zr_{0.3}O_2$ solid solutions. Similar XRD patterns were also observed in mesoporous cubic CeO_2,[57] $Ce_{0.6}Zr_{0.4}O_2$,[58,59] and $Ce_{0.7}Zr_{0.3}O_2$[59] reported by other researchers. By calculating the crystallite sizes via the Scherrer equation, we find that the crystallite sizes of the as-synthesized MgO, γ-Al_2O_3, and $Ce_{1-x}Zr_xO_2$ solid solutions were 4−10, 6−8, and 5−6 nm, respectively, in good agreement with those estimated from their HRTEM images (see later). From the small-angle XRD patterns (Figure 1D) of the MgO, γ-Al_2O_3, and $Ce_{1-x}Zr_xO_2$ samples, it is observed that there was a weak and broad diffraction peak at $2\theta \approx 0.9°$, characteristics of worm-hole-like or poorly ordered mesopores, for each of the MgO and $Ce_{1-x}Zr_xO_2$ samples. The difference in signal intensity among these samples indicates the variation in mesopore structure. The appearance of a relatively sharp diffraction peak (at $2\theta \approx 0.9°$) with higher intensity for the two alumina samples implies the presence of ordered mesopores. The small-angle XRD results demonstrate that adopting PMMA and F127 as the template in ethanol or ethanol−nitric acid solution could

(56) (a) Niu, H.; Yang, Q.; Tang, K.; Xie, Y. *Microporous Mesoporous Mater.* **2006**, *96*, 428. (b) Yu, J. C.; Xu, A.; Zhang, L.; Song, R.; Wu, L. *J. Phys. Chem. B* **2004**, *108*, 64. (c) Li, W.; Lu, A.; Weidenthaler, C.; Schüth, F. *Chem. Mater.* **2004**, *16*, 5676.

(57) Deshpande, A. S.; Pinna, N.; Smarsly, B.; Antonietti, M.; Niedererger, M. *Small* **2005**, *1*, 313.

(58) Vidmar, P.; Fornasiero, P.; Kašpar, J.; Gubitosa, G.; Graziani, M. *J. Catal.* **1997**, *171*, 160.

(59) Sugiura, M. *Catal. Surv. Asia* **2003**, *7*, 77.

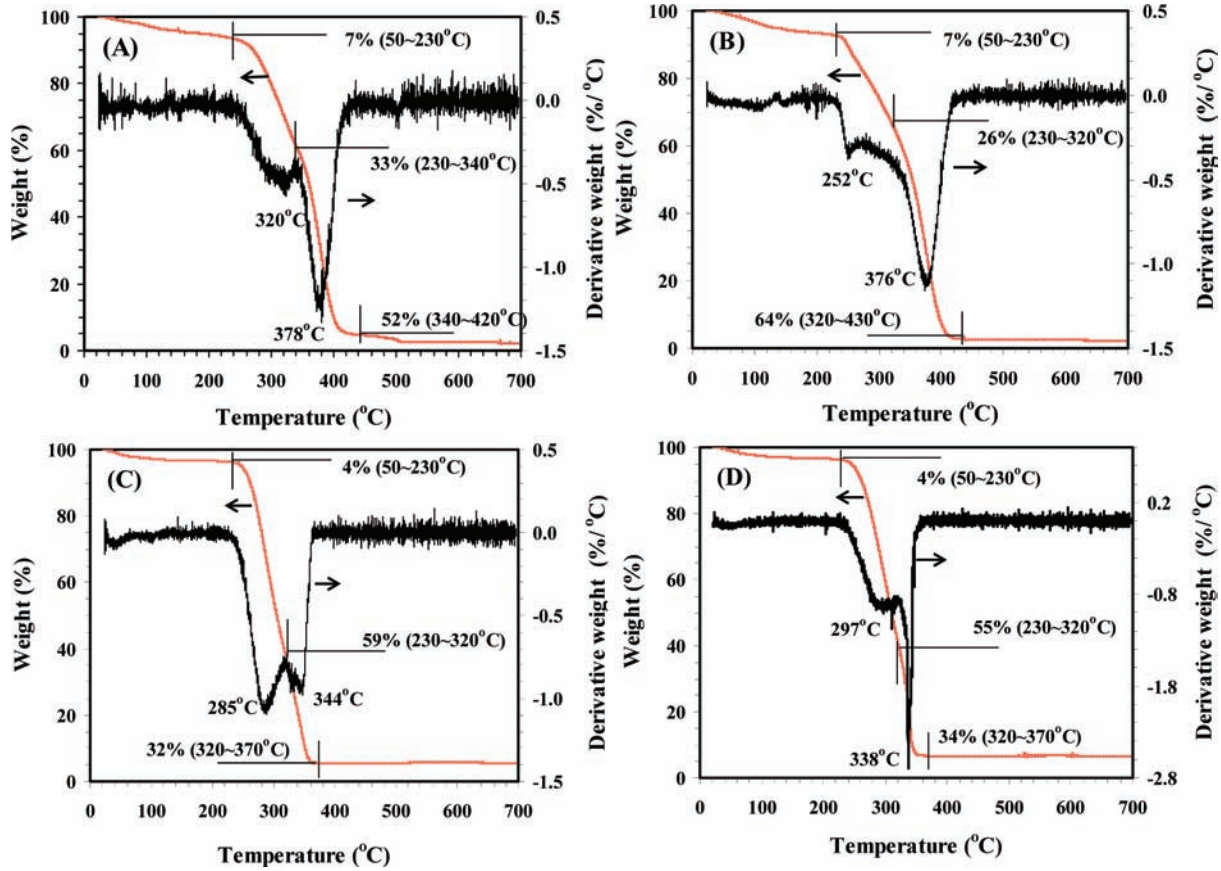

Figure 2. TGA/DSC profiles of (A) MgO obtained with PMMA and F127 in 40% ethanol solution, (B) Al_2O_3 obtained with PMMA and F127 as the template and aluminum nitrate as the Al source in 95% ethanol solution, (C) $Ce_{0.6}Zr_{0.4}O_2$ obtained with PMMA and F127 in 40% ethanol solution, and (D) $Ce_{0.7}Zr_{0.3}O_2$ obtained with PMMA and F127 in 40% ethanol solution before calcination at high temperatures.

fabricate ordered mesoporous alumina with different aluminum precursors, whereas using PMMA as the hard template in the presence or absence of F127 in ethanol or ethanol-free solution resulted in the MgO and $Ce_{1-x}Zr_xO_2$ materials with disordered (worm-hole-like) mesopores.

3.2. Thermal Stability. Figure 2 shows the TGA/DSC profiles of the representative MgO, γ-Al_2O_3, and $Ce_{1-x}Zr_xO_2$ samples before calcination at high temperatures. It is observed from Figure 2A that (i) a gradual small weight loss (ca. 7 wt %) appeared below 230 °C, assignable to the removal of adsorbed water;[60] and (ii) two significant weight losses (ca. 33 and 52 wt %) in the temperature ranges of 230−340 and 340−420 °C, respectively, together with two obvious endothermic peaks at 320 and 378 °C, were detected and both could be related to the decomposition of $Mg(NO_3)_2$ and the removal of PMMA and F127 templates,[45] which was in agreement with the results described elsewhere.[61] Since PMMA microspheres dissociated at ca. 290 °C and oxygenolyzed around 363 °C, we can deduce that the PMMA template could be totally removed below 400 °C. A similar scenario existed in the case of the alumina sample before calcination (Figure 2B): in addition to a weight loss of ca. 7 wt % below 230 °C due to the removal of adsorbed water, there were two weight losses of ca. 26 wt % in the 230−320 °C range and of ca. 64 wt % in the 320−430 °C range due to the thermal decomposition of $Al(NO_3)_3$ and the elimination of the PMMA and F127 templates, corresponding to the endothermic peaks at 252 and 376 °C. For the $Ce_{1-x}Zr_xO_2$ solid solution samples before calcination (Figure 2C and D), the weight loss due to the removal of adsorbed water was less (4 wt %) below 230 °C; the other two weight losses in the ranges of 230−320 and 320−370 °C were 59 and 32 wt % for the uncalcined $Ce_{0.6}Zr_{0.4}O_2$ sample and 55 and 34 wt % for the uncalcined $Ce_{0.7}Zr_{0.3}O_2$ sample, respectively, accompanying by the appearance of two endothermic signals at 285 and 344 °C and at 297 and 338 °C. The weight losses above 230 °C could be ascribable to the decomposition of Ce and Zr nitrates and the removal of PMMA and F127 templates. From Figure 2, one can also observe no further weight loss above 500 °C. This result indicates that the calcination temperatures adopted in the present work are appropriate for the formation of single-phase MgO, γ-Al_2O_3, and $Ce_{1-x}Zr_xO_2$ crystallinites. It is noted that the yields of the 3DOM oxides were 3−7 wt %, similar to or slightly lower than those reported by Stein and co-workers[45,62] and

(60) Wu, Q. Z.; Yi, Q.; Liao, J. F.; Deng, J. H.; Li, Y. G. *Acta Chim. Sin. (in Chinese)* **2005**, *63*, 891.
(61) (a) Yan, H.; Zhang, K.; Blandford, C. F.; Francis, L. F.; Stein, A. *Chem. Mater.* **2001**, *13*, 1374. (b) Yan, H.; Blanford, C. F.; Lytle, J. C.; Carter, C. B.; Smyrl, W. H.; Stein, A. *Chem. Mater.* **2001**, *13*, 4314.
(62) Holland, B. T.; Blanford, C. F.; Do, T.; Stein, A. *Chem. Mater.* **1999**, *11*, 795.
(63) Wu, Q. Z.; Shen, Y.; Li, Y. G. *Acta. Phys.−Chim. Sin. (in Chinese)* **2003**, *19*, 737.

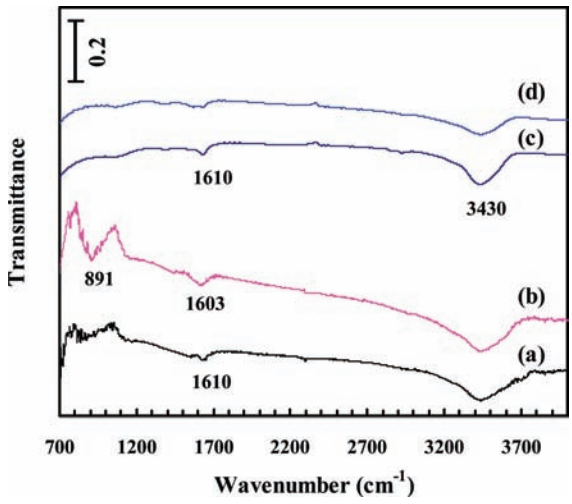

Figure 3. FT-IR spectra of (a) MgO obtained with PMMA and F127 in 40% ethanol solution, (b) γ-Al_2O_3 obtained with PMMA and F127 as the template and $Al(O^iPr)_3$ as the Al source in 95% ethanol−HNO_3 solution, (c) $Ce_{0.6}Zr_{0.4}O_2$ obtained with PMMA and F127 in 40% ethanol solution, and (d) $Ce_{0.7}Zr_{0.3}O_2$ obtained with PMMA and F127 in 40% ethanol solution.

Wu et al.[63] Such a discrepancy in 3DOM metal oxide yield was due to the differences in metal precursor nature and hard and soft templates.

Shown in Figure 3 are the representative FT-IR spectra of the 3DOM MgO, γ-Al_2O_3, and $Ce_{1-x}Zr_xO_2$ samples. It is observed that two absorption bands at 1610 (or 1603) and 3430 cm^{-1} were detected on each sample. Both absorption bands correspond to the stretching and bending vibrations of hydrogen-bonded surface OH groups of the physically adsorbed water.[64] For the alumina sample, the absorption band at 891 cm^{-1} was assigned to the skeletal vibration of Al−O bonds.[65] There were no absorption bands at ca. 3620 cm^{-1} (ascribable to the stretching vibration of bulk OH groups[66]), at ca. 1430 cm^{-1} (due to the symmetric stretching vibration of uni- or bidentate carbonate[67]), and at ca. 870 cm^{-1} (assignable to the carbonate species[68]). In each ceria−zirconia solid solution sample, no absorption bands were recorded at ca. 2820 and 2910 cm^{-1} assignable to the $-CH_2CH_2$ stretching vibrations and at ca. 1060 cm^{-1} due to the C−O stretching vibration of the adopted surfactant molecules or PMMA.[68a] The results indicate that (i) calcining the sample precursors at the adopted temperatures could totally remove the PMMA and F127 templates and (ii) no carbonates are retained in the as-fabricated samples. These outcomes are confirmed by the results of XRD and TGA investigations.

3.3. Pore Structure and Morphology. Figure 4 shows the representative HRSEM images of the MgO samples fabricated under different conditions. It is observed that, in addition to the MgO sample obtained with PMMA and F127 in 95% ethanol solution (Figure 4i), all the other fabricated MgO samples exhibited a 3DOM architecture. Compared to the 3DOM structures of the MgO samples obtained with PMMA but without F127 in aqueous or 95% ethanol solution (Figure 4a and b), the ones obtained with PMMA and F127 in aqueous (Figure 4c and d) or 20−50% ethanol solution (Figure 4e−h) displayed a better alignment of macropores within each entity of MgO, and the 3DOM architecture reached the best in the MgO sample derived with PMMA and F127 in 40% ethanol solution (Figure 4f and g). Further rise in ethanol concentration to 95% resulted in the significant destruction of pore structures (Figure 4i). Shown in Figure 5 are the HRTEM images and SAED pattern of MgO obtained under various conditions. Obviously, the entities of MgO derived with PMMA and/or F127 either in aqueous or in ethanol solution displayed a 3DOM architecture, with the MgO sample obtained with PMMA and F127 in 95% ethanol solution being the exception in which only worm-hole-like mesopores formed between nanoparticles existed. One can also see that the walls of the 3DOM MgO entities were composed of nanoparticles with relatively uniform sizes. The nanoparticles of the 3DOM walls in the MgO samples fabricated with PMMA in the absence of surfactant F127 (Figure 5b and d) were much bigger than those in the MgO samples fabricated with PMMA in the presence of F127 (Figure 5f, h, j, k, m, and o), with the typical particle size range being 15−30 nm for the former and 5−8 nm for the latter. It can also be observed that there was presence of worm-hole-like mesopores (diameter = 2−4 nm) within the walls of the macropores for these MgO samples. These results reveal that (i) the introduction of F127 facilitates the formation of MgO nanoparticles with smaller and more uniform size; (ii) there is the presence of an optimal ethanol concentration (40%) for the generation of high-quality 3DOM structure; and (iii) worm-hole-like mesopores exist within the walls of the 3DOM entities. The recording of several bright and well-resolved electron diffraction rings (inset of Figure 5k) for the 3DOM MgO sample obtained with PMMA and F127 in 40% ethanol solution demonstrates the formation of polycrystalline structure. Similar results were also obtained for the MgO samples fabricated under the other synthesis conditions. It deserves to be mentioned that, with PMMA and F127 as the template and magnesium nitrate rather than magnesium acetate as the Mg source in a 100% ethanol solution, one could only obtain spongelike polycrystalline MgO samples (Figure S2 of the Supporting Information); with PMMA and F127 as the template and magnesium nitrate as the Mg source in a 40% ethanol solution, if this mixed solution was dried in an environment with a relative humility of 60% and then calcined at 550 °C for 5 h, one could only obtain polycrystalline MgO nanoparticles with a tetragonal morphology (Figure S3 of the Supporting Information).

Figure 6 shows the HRSEM and HRTEM photographs as well as the SAED pattern of the γ-Al_2O_3 samples synthesized with PMMA and F127 and different Al precursors in various solutions. It is observed that all the alumina samples

(64) Gadsden, J. A. *Infrared Spectra of Minerals and Related Inorganic Compounds*; Butterworths: London, UK, 1975.
(65) Parida, K. M.; Pradhan, A. C.; Das, J.; Sahu, N. *Mater. Chem. Phys.* **2009**, *113*, 244.
(66) Echterhoff, R.; Hoffmann, P.; Knözinger, E. *Surface structures of silica, magnesia, and calcium oxide studied by modern IR spectroscopy*, Proceedings of the 9th International Congress on Catalysis, Calgary, June 26 to July 2, 1988; p 1418.
(67) Philipp, R.; Fujimoto, K. *J. Phys. Chem.* **1992**, *96*, 9035.
(68) (a) Thierry, B.; Zimmer, L.; McNiven, S.; Finnie, K.; Barbé, C.; Griesser, H. J. *Langmuir* **2008**, *24*, 8143. (b) Busca, G.; Lorenzelli, V. *Mater. Chem.* **1982**, *7*, 89.

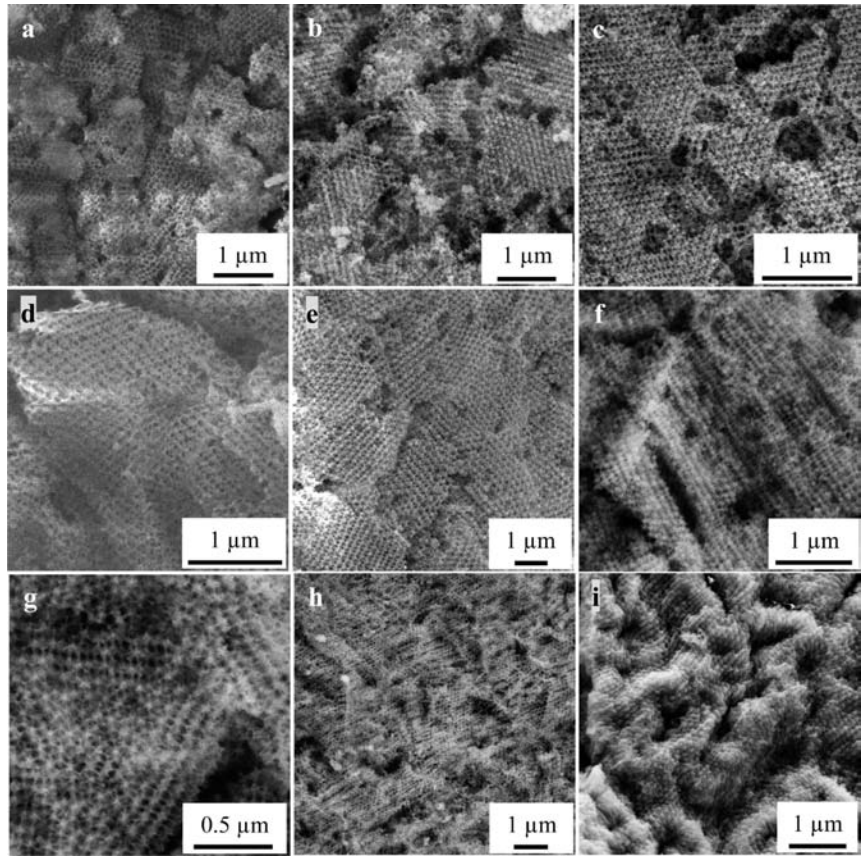

Figure 4. HRSEM images of MgO obtained with (a) PMMA in aqueous solution, (b) PMMA in 95% ethanol solution, (c and d) PMMA and F127 in aqueous solution, (e) PMMA and F127 in 20% ethanol solution, (f and g) PMMA and F127 in 40% ethanol solution, (h) PMMA and F127 in 50% ethanol solution, and (i) PMMA and F127 in 95% ethanol solution.

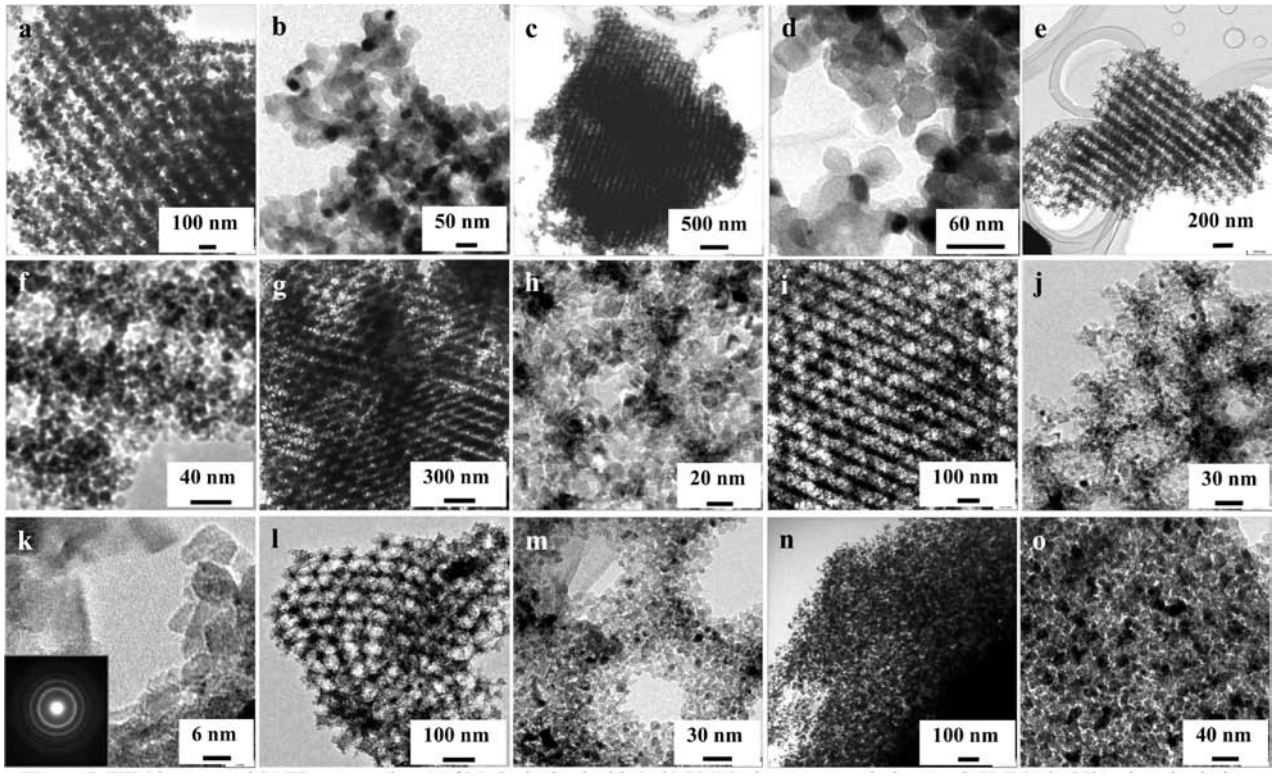

Figure 5. TEM images and SAED pattern (inset) of MgO obtained with (a and b) PMMA in aqueous solution, (c and d) PMMA in 95% ethanol solution, (e and f) PMMA and F127 in aqueous solution, (g and h) PMMA and F127 in 20% ethanol solution, (i−k) PMMA and F127 in 40% ethanol solution, (l and m) PMMA and F127 in 50% ethanol solution, and (n and o) PMMA and F127 in 95% ethanol solution.

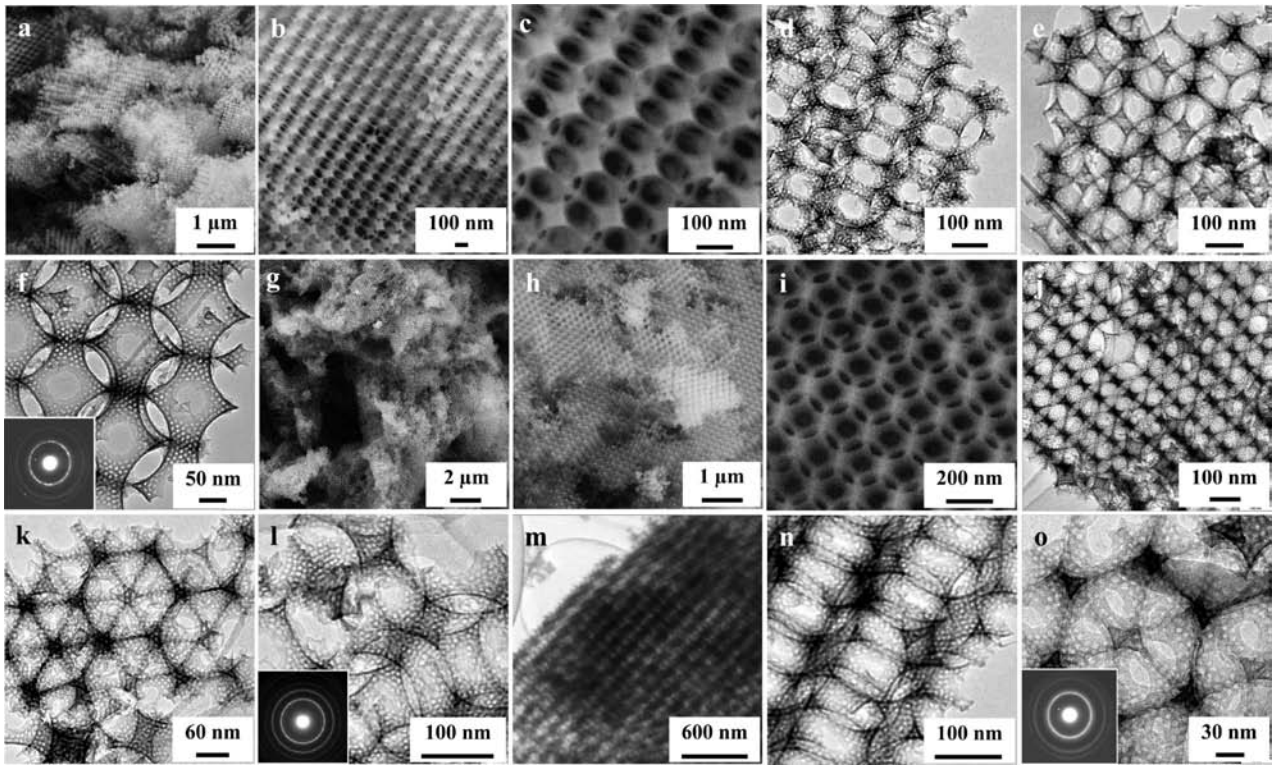

Figure 6. HRSEM and TEM images as well as SAED patterns (insets) of γ-Al_2O_3 obtained with PMMA and F127 as the template and (a−f) aluminum nitrate as the Al source in 95% ethanol solution and (g−l) $Al(O^iPr)_3$ as the Al source in 95% ethanol−HNO_3 solution and (m−o) in 95% ethanol−HCl solution.

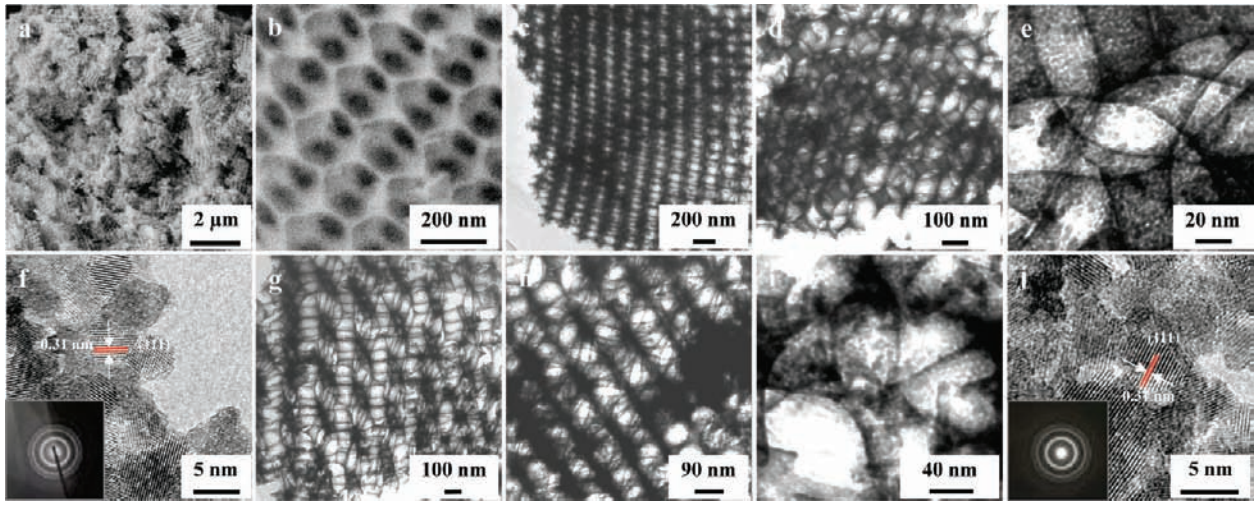

Figure 7. HRSEM and TEM images as well as SAED patterns (insets) of (a−f) $Ce_{0.6}Zr_{0.4}O_2$ obtained with PMMA and F127 in 40% ethanol solution and (g−j) $Ce_{0.7}Zr_{0.3}O_2$ obtained with PMMA and F127 in 40% ethanol solution.

displayed a highly ordered macroporous structure with the macropore size of 53−171 nm; meanwhile, there was formation of 3D ordered mesopores within the walls (thickness, 10−80 nm) of the macropores, which was confirmed by the small-angle XRD results. The mesopore diameters were in the range of 4−8 nm. These results indicate that the nature of aluminum precursor or inorganic acid added in the ethanol solution had no significant impact on the macroporous structure of the alumina product, but it gave rise to the change in mesopore structure, which was reflected by the surface areas (see later). From the SAED patterns (Figure 6f, l, and o), one can see multiple bright electron diffraction rings, meaning that the three γ-alumina samples were polycrystalline.

Shown in Figure 7 are the HRSEM and HRTEM images as well as SAED patterns of $Ce_{1-x}Zr_xO_2$ derived with PMMA and F127 in 40% ethanol solution. It is apparent that highly 3D ordered macroporous architectures were generated in both ceria−zirconia solid solution samples; the walls of micropores were constituted by a number of $Ce_{1-x}Zr_xO_2$ nanocrystals, among which numerous worm-hole-like mesopores with a pore diameter of ca. 3 nm were formed. The typical size of the nanocrystals was 4−7 nm for the

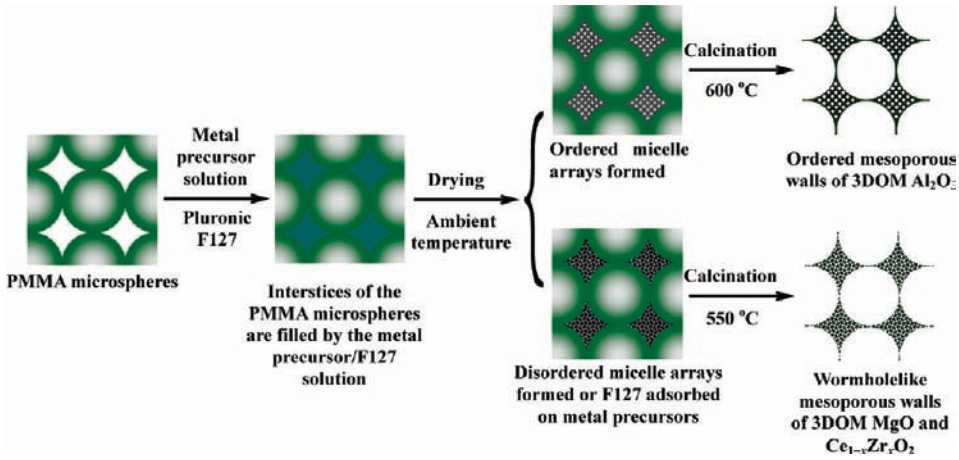

Figure 8. Schematic illustration of formation mechanisms of the 3DOM MgO, γ-Al_2O_3, and $Ce_{1-x}Zr_xO_2$ samples with crystalline mesoporous walls.

$Ce_{0.6}Zr_{0.4}O_2$ sample (Figure 7f) and the $Ce_{0.7}Zr_{0.3}O_2$ sample (Figure 7i). From the HRTEM images of both samples, one can see the well-resolved (111) plane with the *d* spacing of ca. 0.31 nm, which was in good agreement with that (0.306400 nm) of standard $Ce_{0.6}Zr_{0.4}O_2$ (JCPDS PDF no. 38-1439). The observation of at least three bright electron diffraction rings in the SAED patterns of the two samples revealed the formation of polycrystallites (Figure 7f and i). It should be noted that the theoretical Ce:Zr molar ratio of $Ce_{0.6}Zr_{0.4}O_2$ and $Ce_{0.7}Zr_{0.3}O_2$ is 6/4 (i.e., 1.5/1) and 7/3 (i.e., 2.33/1), respectively. From the quantitative data obtained from the EDXS spectra (Figure S4 of the Supporting Information), one can see that the Ce:Zr molar ratio was 11.99/7.59 (i.e., 1.58/1.00) for the $Ce_{0.6}Zr_{0.4}O_2$ sample obtained with PMMA and F127 in 40% ethanol solution, and 17.91/7.97 (i.e., 2.25/1.00) for the $Ce_{0.7}Zr_{0.3}O_2$ sample obtained with PMMA and F127 in 40% ethanol solution. Both were rather close to the theoretical Ce:Zr molar ratio (1.5/1 and 2.33/1, respectively). Such a discrepancy might be due to the presence of experimental error in the EDXS measurements.

It should be noted that the macropore (void formed due to PMMA removal) diameter of the fabricated oxide depends upon the size of the PMMA microspheres. The void diameters were about 160, 175, 190, and 200 nm for the as-synthesized MgO, γ-Al_2O_3 $Ce_{0.6}Zr_{0.4}O_2$, and $Ce_{0.7}Zr_{0.3}O_2$ samples, respectively. Comparing to the average size (ca. 298 nm) of PMMA colloidal crystal microspheres used as the hard template, the macropore diameter exhibited a shrinkage of 30−44%, which was basically consistent with the 26−34% contraction ratio of macroporous SiO_2, TiO_2, ZrO_2, and Al_2O_3 fabricated by means of a similar method.[62,69] Although the removal of the PMMA template as well as the F127 surfactant via calcination resulted in such a big shrinking in macropore size, well-structured 3DOM entities were still retained. Figure 8 illustrates the formation mechanisms of the 3DOM oxides with crystalline mesoporous walls. It describes an evaporation-induced self-assembly process, in which, with the gradual removal of solvent (water or ethanol) upon drying, the concentration of surfactant F127 rises to a value higher than the critical micelle concentration[70] and the mesoporous structure is hence formed. The aqueous or ethanol solution containing F127 and Mg, Al, or Ce and Zr nitrate(s) or $Al(O^iPr)_3$ first fills up the interstices of the well-arrayed PMMA colloidal crystal microspheres, in which via the interaction of the precursor with the surfactant there is formation of micelles in an ordered or disordered array. After being dried at ambient temperature, the metal precursor(s) and surfactant display an ordered or disordered packing within the voids between the PMMA microspheres. By removing the PMMA and F127 via calcination of the dried sample at 550 or 600 °C, one can obtain the 3DOM γ-Al_2O_3 with ordered mesoporous walls or 3DOM MgO and $Ce_{1-x}Zr_xO_2$ with worm-hole-like mesoporous walls. Similar formation pathways have been discussed by other researchers.[45,52] In addition to the role of the micelles in the formation of 3DOM MgO and 3DOM $Ce_{1-x}Zr_xO_2$, it is also possible that in these samples the surfactant molecules adsorbed on the metal precursors and hence inhibited the growth of metal (mixed) oxide particles. A piece of supporting evidence was from the fact that the particle grain sizes were much smaller in the final products for which F127 was employed. The TEM images (Figures 5 and 7) showed the presence of textural mesopores between adjacent nanoparticles in the 3DOM MgO and 3DOM $Ce_{1-x}Zr_xO_2$ samples, in which the mesopore architecture might be controlled more by oxide crystallization effects than by surfactant templating.

Figure 9 shows the N_2 adsorption−desorption isotherms and pore size distributions of 3DOM MgO, γ-Al_2O_3, and $Ce_{1-x}Zr_xO_2$ synthesized under different conditions. From Figure 9A, one can find that the isotherms of all the 3DOM samples exhibited type II characteristic of a type H3 hysteresis loop in the relative pressure (p/p_0) range of 0.8−1.0 as well as a small H2 type hysteresis loop in the p/p_0 range of 0.2−0.8. The type H3 loop, which does not clearly exhibit any adsorption plateau at relative pressures close to unity, is usually related to the existence of slit-shaped pores in materials, indicative of a pore size distribution extending to the macropore range.[56c] The low-pressure portion of the

(69) Holland, B. T.; Blanford, C. F.; Stein, A. *Science* **1998**, *281*, 538.

(70) Lu, Y.; Gangull, R.; Drewien, C. A.; Anderson, M. T.; Brinker, C. J.; Gong, W.; Huang, M. H.; Zink, J. I. *Nature (London)* **1997**, *389*, 364.

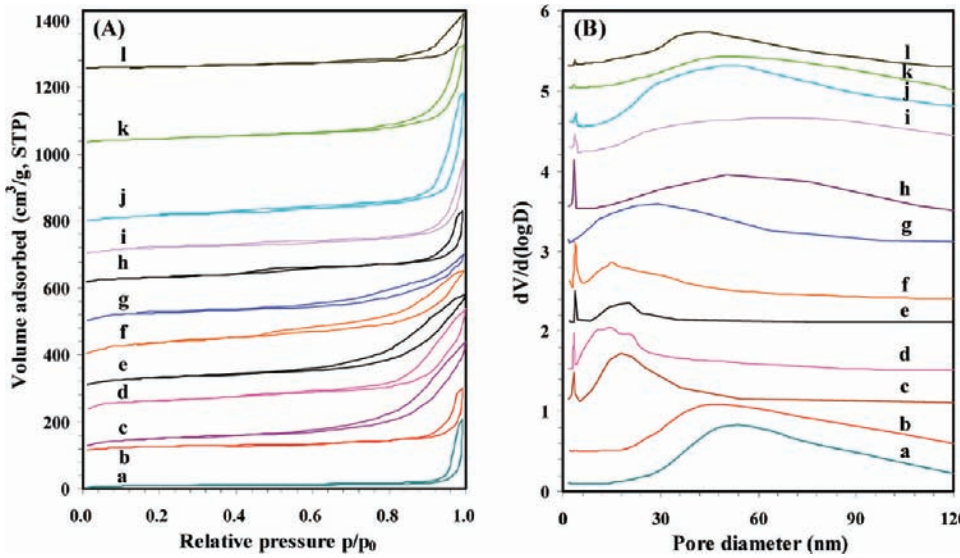

Figure 9. (A) Nitrogen adsorption−desorption isotherms and (B) pore size distribution curves of MgO obtained with (a) PMMA in aqueous solution, (b) PMMA in 95% ethanol solution, (c) PMMA and F127 in aqueous solution, (d) PMMA and F127 in 20% ethanol solution, (e) PMMA and F127 in 40% ethanol solution, (f) PMMA and F127 in 50% ethanol solution, and (g) PMMA and F127 in 95% ethanol solution; γ-Al_2O_3 obtained with PMMA and F127 as the template and (h) aluminum nitrate as the Al source in 95% ethanol solution and $Al(O^iPr)_3$ as the Al source (i) in 95% ethanol−HNO_3 solution and (j) in 95% ethanol−HCl solution; (k) $Ce_{0.6}Zr_{0.4}O_2$ obtained with PMMA and F127 in 40% ethanol solution and (l) $Ce_{0.7}Zr_{0.3}O_2$ obtained with PMMA and F127 in 40% ethanol solution.

Table 1. BET Surface Areas and Pore Volumes of the Fabricated 3DOM MgO, γ-Al_2O_3, and $Ce_{1-x}Zr_xO_2$ Samples

					BET surface area (m^2/g)			pore volume (cm^3/g)		
sample	hard/soft templates	metal source	solvent	calcination condition	macropore (>40 nm)	mesopore (≤40 nm)	total	macropore (>40 nm)	mesopore (≤40 nm)	total
MgO	PMMA/−	$Mg(NO_3)_2$	water	300 °C 3 h, 550 °C 5 h	17	18	35	0.27	0.05	0.32
MgO	PMMA/−	$Mg(NO_3)_2$	95% ethanol	300 °C 3 h, 550 °C 5 h	16	23	39	0.24	0.10	0.34
MgO	PMMA/F127	$Mg(NO_3)_2$	water	300 °C 3 h, 550 °C 5 h	7	155	162	0.03	0.33	0.36
MgO	PMMA/F127	$Mg(NO_3)_2$	20% ethanol	300 °C 3 h, 550 °C 5 h	12	171	183	0.09	0.34	0.43
MgO	PMMA/F127	$Mg(NO_3)_2$	40% ethanol	300 °C 3 h, 550 °C 5 h	5	238	243	0.06	0.39	0.45
MgO	PMMA/F127	$Mg(NO_3)_2$	50% ethanol	300 °C 3 h, 550 °C 5 h	8	172	180	0.09	0.40	0.49
MgO	PMMA/F127	$Mg(NO_3)_2$	95% ethanol	300 °C 3 h, 550 °C 5 h	10	124	125	0.14	0.35	0.49
γ-Al_2O_3	PMMA/F127	$Al(NO_3)_3 \cdot 9H_2O$	95% ethanol	300 °C 3 h, 600 °C 5 h	10	108	118	0.16	0.20	0.36
γ-Al_2O_3	PMMA/F127	$Al(O^iPr)_3$	95% ethanol−HNO_3	300 °C 3 h, 600 °C 5 h	18	127	145	0.17	0.28	0.45
γ-Al_2O_3	PMMA/F127	$Al(O^iPr)_3$	95% ethanol−HCl	300 °C 3 h, 600 °C 5 h	19	117	136	0.34	0.34	0.68
$Ce_{0.6}Zr_{0.4}O_2$	PMMA/F127	$Ce(NO_3)_3 \cdot 6H_2O$ $ZrO(NO_3)_2 \cdot 2H_2O$	40% ethanol	300 °C 3 h, 550 °C 6 h	19	81	100	0.27	0.24	0.51
$Ce_{0.7}Zr_{0.3}O_2$	PMMA/F127	$Ce(NO_3)_3 \cdot 6H_2O$ $ZrO(NO_3)_2 \cdot 2H_2O$	40% ethanol	300 °C 3 h, 550 °C 6 h	14	77	91	0.08	0.25	0.33

almost linear middle section of the isotherm, which is attributed to unrestricted mono- or multilayer adsorption, suggests that the sample was a macroporous adsorbent.[45] However, the small H2 type hysteresis loop in the p/p_0 range of 0.2−0.8, linkable to capillary condensation taking place in mesopores, indicates that textural mesopores existed within the wall structure.[45,56c,71] The isotherms as well as hysteresis loops between the p/p_0 range of 0.45−1.0 were much more similar to those of mesoporous MgO samples reported by Gulková et al.[72] There is a discrepancy in the shape and p/p_0 range of the H2 type hysteresis loop for the oxide samples, implying the existence of difference in mesopore structure. Among these 3DOM oxide samples, the γ-Al_2O_3 ones displayed much more clearly observable H2 type hysteresis loops, indicating the generation of much better mesoporous architecture. This was confirmed by the results of HRTEM investigations. From Figure 9B, one can observe that the MgO samples obtained with PMMA and F127-free aqueous or 95% ethanol solution or with PMMA and F127 in 95% ethanol solution exhibited only a rather broad pore size distribution (centered at 54, 45, and 30 nm, respectively); for all the other samples, however, there were two pore size distributions: one narrow peak centered at 3−5 nm and one broad peak centered at 15−60 nm which varied from sample to sample.

3.4. Surface Area and Pore Volume. The BET surface areas and pore volumes of the MgO, γ-Al_2O_3, and $Ce_{1-x}Zr_xO_2$ samples synthesized under different conditions are summarized in Table 1. It can be seen that, in the absence of F127, the MgO samples obtained with PMMA either in aqueous or in 95% ethanol solution exhibited low surface areas (35−39 m^2/g) and medium pore volumes (0.32−0.34 cm^3/g); the surface areas of marcopores and mesopores were similar, but the pore volume of marcopores was much higher

(71) (a) Yang, C.; Schmidt, W.; Kleitz, F. *J. Mater. Chem.* **2005**, *15*, 5112. (b) Chen, D.; Li, Z.; Wan, Y.; Tu, X.; Shi, Y.; Chen, Z.; Shen, W.; Yu, C.; Tu, B.; Zhao, D. *J. Mater. Chem.* **2006**, *16*, 1511. (c) Matos, J. R.; Kruk, M.; Mercuri, L. P.; Jaroniec, M.; Zhao, L.; Kamiyama, T.; Terasaki, O.; Pinnavaia, T. J.; Liu, Y. *J. Am. Chem. Soc.* **2003**, *125*, 821.

(72) Gulková, D.; Šolcová, O.; Zdražil, M. *Microporous Mesoporous Mater.* **2004**, *76*, 137.

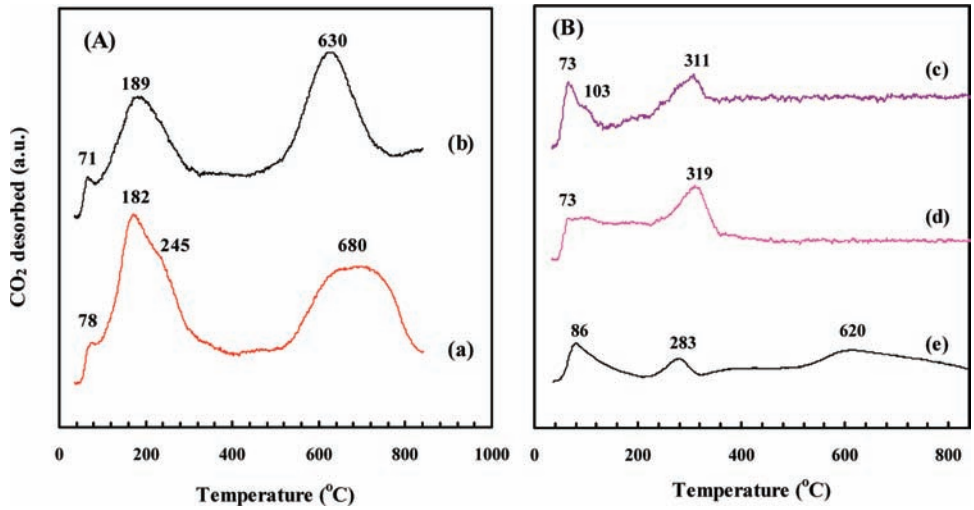

Figure 10. CO_2-TPD profiles of (A) 3DOM MgO obtained with PMMA and F127 in (a) 20% ethanol solution and (b) 40% ethanol solution and (B) 3DOM γ-Al_2O_3 obtained with PMMA and F127 as the template and $Al(O^iPr)_3$ as the Al source in (c) 95% ethanol−HCl solution, (d) 95% ethanol−HNO_3 solution, and (e) the commercial γ-Al_2O_3 sample.

than that of mesopores for each of the two samples. In the presence of F127, the MgO samples obtained with PMMA in various ethanol solutions possessed much higher surface areas (125−243 m^2/g), with the highest value over the MgO sample derived with PMMA in 40% ethanol solution; a further rise in ethanol concentration gave rise to a marked drop in surface area; the pore volumes of the MgO samples increased considerably. It is worthwhile to point out that the introduction of surfactant (soft template) F127 enhanced the surface areas of the 3DOM MgO samples (125−243 m^2/g), which were much higher than that (35 m^2/g) of the MgO sample fabricated with PS as the hard template in the absence of a surfactant after calcination at 500 °C.[45] The obvious positive effect of F127 on the enhancement in surface area of the 3DOM materials is due to the formation of mesopore structure within the walls. Unlike the case of the F127-free derived MgO samples, remarkable contributions to large surface areas and pore volumes in the F127-added derived MgO samples were from the mesopores. For the 3DOM γ-Al_2O_3 samples, the surface areas and pore volumes were in the ranges of 118−145 m^2/g and 0.36−0.68 cm^3/g, respectively; the gamma-alumina sample obtained with PMMA and F127 in 95% ethanol−nitric acid solution displayed the highest surface area whereas the gamma-alumina sample fabricated with PMMA and F127 in 95% ethanol−hydrochloric acid solution possessed the largest pore volume. For the $Ce_{1-x}Zr_xO_2$ samples, the surface areas and pore volumes were 91−100 m^2/g and 0.33−0.51 cm^3/g, respectively.

3.5. CO_2 Adsorption Behavior. Figure 10 shows the CO_2-TPD profiles of the MgO and γ-Al_2O_3 samples fabricated under different conditions. It is observed from Figure 10A that there were two kinds of CO_2 desorption: the low-temperature desorption in the range of 60−320 °C and the high-temperature desorption in the range of 500−800 °C, assignable to weak chemisorption and strong chemisorption, respectively. Such a two-stepped CO_2 desorption pattern for alkaline oxides was also reported by Hattori and co-workers[73] and Yanagisawa et al.[74] The desorption temperatures of CO_2 from the 3DOM MgO samples were similar to those from the macroporous CaO (surface area = 139 m^2/g)[75] and worm-hole-like mesoporous CaO (surface area = 110−257 m^2/g) samples.[76] In the low-temperature desorption region, there was one main desorption peak centered at 180−189 °C with two shoulders at 71−78 and 245 °C ascribable to weakly chemisorbed CO_2 species, and the desorption amount of CO_2 was 216 μmol/g for the 3DOM MgO sample obtained with PMMA and F127 in 20% ethanol solution and 319 μmol/g for the 3DOM MgO sample obtained with PMMA and F127 in 40% ethanol solution. The maximal temperature for desorption of strongly chemisorbed CO_2 species from the former sample was ca. 50 °C lower than that from the latter sample, and the desorption amount of CO_2 was 200 and 248 μmol/g, respectively. Thus, the total amount of CO_2 desorbed from the 3DOM MgO samples derived with PMMA and F127 as the template in 20 and 40% ethanol solutions was accordingly 416 and 568 μmol/g; such a sequence coincides with that of the surface area of the two samples. The CO_2 desorption amounts of the 3DOM MgO samples are much higher than the CO_2 uptake (ca. 307 μmol/g) of the CaO sample (surface area, 30.7 m^2/g)[67] and even nearly an order of magnitude higher than that (54−79 μmol/g) of the porous CaO sample (surface area, 19 m^2/g) which was sintered at 686 °C for 100 h,[77] although they are lower as compared to those (730−770 μmol/g) of mesoporous CaO (surface area 221−257 m^2/g) reported by our group.[76]

There are rare reports on the CO_2 adsorption property of gamma-alumina in the literature due to its weak basicity.

(73) (a) Zhang, G.; Hattori, H.; Tanabe, K. *Appl. Catal.* **1988**, *36*, 189. (b) Hattori, H. *Chem. Rev.* **1995**, *95*, 537.
(74) Yanagisawa, Y.; Takaoka, K.; Yamabe, S. *J. Phys. Chem.* **1995**, *99*, 3704.
(75) Liu, S.; Huang, S.; Li, J.; Zhao, N.; Wei, W.; Sun, Y. *Petrochem. Technol. (in Chinese)* **2007**, *36*, 1250.
(76) Liu, C.; Zhang, L.; Deng, J.; Mu, Q.; Dai, H.; He, H. *J. Phys. Chem. C* **2008**, *112*, 19248.
(77) Beruto, D.; Botter, R.; Seary, A. W. *J. Phys. Chem.* **1984**, *88*, 4052.

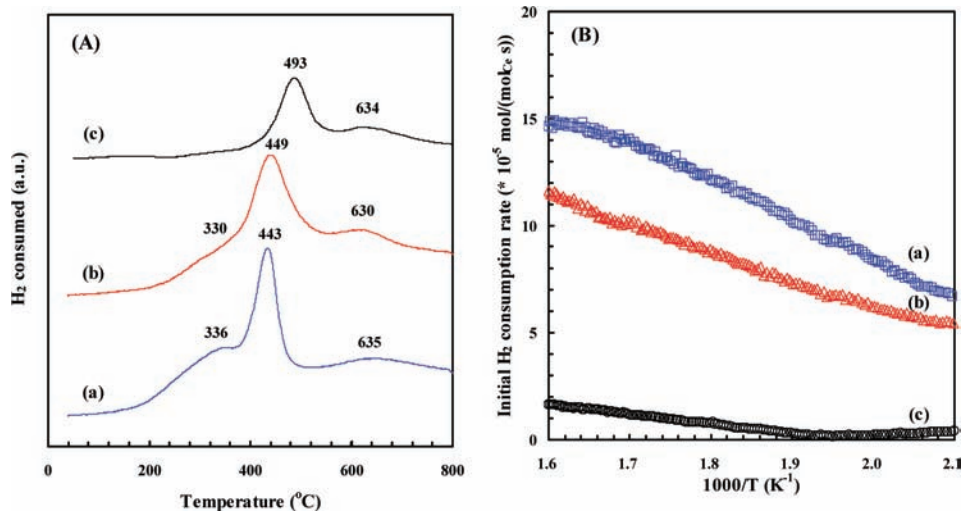

Figure 11. (A) H_2-TPR profiles and (B) initial H_2 consumption rate of (a) 3DOM $Ce_{0.6}Zr_{0.4}O_2$ obtained with PMMA and F127 in 40% ethanol solution, (b) 3DOM $Ce_{0.7}Zr_{0.3}O_2$ obtained with PMMA and F127 in 40% ethanol solution, and (c) $Ce_{0.7}Zr_{0.3}O_2$ nanoparticles obtained using the coprecipitation method.

γ-Al_2O_3 is often used as a catalyst support for a number of CO_2-involving reactions. In this case, the CO_2 sorption behavior of γ-Al_2O_3 support would have an impact on its catalytic performance. Shown in Figure 10B are the CO_2-TPD profiles of the 3DOM γ-Al_2O_3 and commercial γ-Al_2O_3 (surface area = 104 m^2/g, Beijing Chemical Reagent Company) samples. For each sample, two CO_2 desorption signals at 73−86 and 283−86 °C were detected; the former was attributed to weakly adsorbed CO_2 species, whereas the latter was assigned to strongly adsorbed CO_2 species: another weak and broad desorption signal centered at 620 °C appeared for the commercial γ-Al_2O_3 sample, ascribable to the formation of carbonate. Such a high-temperature desorption due to carbonate formation is a shortcoming of γ-Al_2O_3 when it is employed as a support because it would undermine the catalyst stability. In view of this phenomenon, the commercial γ-Al_2O_3 is inferior to its 3DOM-structured counterparts. The total CO_2 desorption amount below 400 °C was 158 μmol/g for the 3DOM γ-Al_2O_3 sample obtained with PMMA and F127 as the template and Al(O^iPr)$_3$ as the Al source in 95% ethanol−HCl solution, 259 μmol/g for the 3DOM γ-Al_2O_3 sample obtained with PMMA and F127 as the template and Al(O^iPr)$_3$ as the Al source in 95% ethanol−HNO_3 solution, and 91 μmol/g for the commercial γ-Al_2O_3 sample. Apparently, the two 3DOM γ-Al_2O_3 samples exhibited higher CO_2 desorption amounts than the commercial γ-Al_2O_3 sample. The presence of 3D macropores and ordered mesopores in γ-Al_2O_3 obtained in the present study may facilitate the adsorption, desorption, and diffusion of CO_2 molecules, partly contributing to the enhanced CO_2 adsorption ability. Therefore, we believe that, compared to the commercial γ-Al_2O_3, the as-fabricated 3DOM-structured γ-Al_2O_3 samples are more suitable for the use as support or CO_2 adsorbent.

3.6. Reducibility. TPR experiments were conducted to evaluate the reducibility of as-fabricated 3DOM $Ce_{1-x}Zr_xO_2$ and coprecipitation-derived $Ce_{0.7}Zr_{0.3}O_2$ (Figure S5 of the Supporting Information) samples, and the results are illustrated in Figure 11. Two reduction processes were observed for each sample: one at 200−550 °C and the other at 550−800 °C (Figure 11A). In the case of the 3DOM $Ce_{0.6}Zr_{0.4}O_2$ or 3DOM $Ce_{0.7}Zr_{0.3}O_2$ samples, the appearance of one main reduction band at 440−450 °C with a shoulder at 330−336 °C implies the existence of at least two kinds of cerium species at various coordination environments; in the case of the $Ce_{0.7}Zr_{0.3}O_2$ nanoparticle sample fabricated by means of the coprecipitation strategy, however, the first reduction band appeared at a higher temperature (ca. 50 °C higher than that over the 3DOM ceria−zirconia solid solutions). The reduction band at low temperature could be attributed to the reduction of surface Ce^{4+} to Ce^{3+} as well as the removal of surface oxygen adspecies,[36,78] and the H_2 consumption was 311, 293, and 133 mmol/mol$_{Ce}$ for the 3DOM $Ce_{0.6}Zr_{0.4}O_2$, 3DOM $Ce_{0.7}Zr_{0.3}O_2$, and $Ce_{0.7}Zr_{0.3}O_2$ nanoparticle samples, respectively; the reduction band at high temperature could be ascribed to the reduction of bulk Ce^{4+} to Ce^{3+},[36,78] and the corresponding H_2 consumption was 105, 102, and 57 mmol/mol$_{Ce}$. The results indicate that the reducibility at lower temperatures (200−550 °C) increased in the order of $Ce_{0.7}Zr_{0.3}O_2$ nanoparticles < 3DOM $Ce_{0.7}Zr_{0.3}O_2$ < 3DOM $Ce_{0.6}Zr_{0.4}O_2$. For the sake of better comparison for the reducibility of the ceria−zirconia solid solution samples, we use the initial H_2 consumption rate in the reduction temperature range of 200−350 °C (corresponding to less than ca. 25% H_2 consumption of the low-temperature reduction band) where no phase transformation took place, and the results were shown in Figure 11B. It is clear that the initial H_2 consumption rate follows an order

(78) (a) Jacobs, G.; Graham, U. M.; Chenu, E.; Patterson, P. M.; Dozier, A.; Davis, B. H. *J. Catal.* **2005**, *229*, 499. (b) Di Monte, R.; Fornasiero, P.; Graziani, M.; Kašpar, J. *J. Alloys Compd.* **1998**, *275−277*, 877. (c) Markaryan, G. L.; Ikryannikova, L. N.; Muravieva, G. P.; Turakulova, A. O.; Kostyuk, B. G.; Lunina, E. V.; Lunin, V. V.; Zhilinskaya, E.; Aboukaïs, A. *Colloids Surf. A* **1999**, *151*, 435. (d) Kulyova, S. P.; Lunina, E. V.; Lunin, V. V.; Kostyuk, B. G.; Muravyova, G. P.; Kharlanov, A. N.; Zhilinskaya, E. A.; Aboukaïs, A. *Chem. Mater.* **2001**, *13*, 1491. (e) Masui, T.; Peng, Y.; Machida, K.-I.; Adachi, G.-Y. *Chem. Mater.* **1998**, *10*, 4005. (f) Ozaki, T.; Masui, T.; Machida, K.-I.; Adachi, G.-Y.; Sakata, T.; Mori, H. *Chem. Mater.* **2000**, *12*, 643.

of 3DOM $Ce_{0.6}Zr_{0.4}O_2$ > 3DOM $Ce_{0.7}Zr_{0.3}O_2$ ≫ $Ce_{0.7}Zr_{0.3}O_2$ nanoparticles. Such a sequence of initial H_2 consumption rate is in good agreement with the H_2 consumption at low temperature of the ceria−zirconia solid solution samples. It can be inferred from these results that there is presence of morphology-dependent reducibility for the $Ce_{1-x}Zr_xO_2$ samples. Similar morphological effect on the reduction property of CeO_2 has also been reported in the literature.[79−82] After examining the reducibility of CeO_2 with various morphologies, Yang et al. observed that the H_2 consumption of cubelike ceria nanoparticles was 4−5 times higher than that of irregular CeO_2 particles, and they attributed the enhancement in reducibility to the peculiar particle morphology of ceria.[82a] Working on the fabrication and catalytic properties of spindlelike, rodlike, and spherical ceria for CO oxidation, Yu and co-workers pointed out that the different morphologies led to various oxygen vacancies and Ce^{4+} reduction extents of CeO_2, hence directly influencing their catalytic performance for the addressed reaction.[80] The experimental H_2 consumptions of the 3DOM $Ce_{1-x}Zr_xO_2$ samples (293−311 $mmol/mol_{Ce}$) are much higher than those of CeO_2 nanotubes (130 $mmol/mol_{Ce}$)[82b] and CeO_2 nanoparticles (19 $mmol/mol_{Ce}$).[79] Although the experimental H_2 consumptions of our 3DOM $Ce_{1-x}Zr_xO_2$ samples are close to or lower than those of the CeO_2−ZrO_2 samples with different Ce/Zr or Pr/Zr atomic ratios (220−448 $mmol/mol_{Ce}$) reported by Narula et al.,[83] the onsets of the low-temperature reduction of the former samples (around 200 °C) are much lower than those of the latter samples (above 400 °C). We think that the excellent low-temperature reducibility of 3DOM $Ce_{1-x}Zr_xO_2$ is associated with the unique 3D architecture (which is favorable for the diffusion of H_2 molecules) and the uniform and small-sized solid solution nanoparticles (more surface Ce^{4+} ions which are accessible to H_2 molecules).

4. Conclusions

With magnesium, aluminum, cerium and zirconium nitrates, or $Al(O^iPr)_3$ as the metal source, close-packed PMMA colloidal crystal microspheres as the hard template, triblock copolymer F127 as the surfactant (soft template), we fabricated 3DOM-structured MgO and $Ce_{1-x}Zr_xO_2$ ($x = 0.3$, 0.4) solid solutions with worm-hole-like mesoporous crystalline walls and 3DOM-structured γ-Al_2O_3 with 3D ordered mesoporous crystalline walls. The solvent (ethanol or water) and concentration, metal precursor, surfactant, and drying condition are factors influencing the pore structures of the 3DOM products. We found that adding surfactant F127 to the fabrication system could markedly enhance the surface areas of the 3DOM metal oxides. It is observed that (i) with PMMA and F127 as the template in a 40% ethanol solution, one can obtain 3DOM-structured MgO with the highest surface area of 243 m^2/g and 3DOM-structured $Ce_{0.6}Zr_{0.4}O_2$ with the highest surface area of 100 m^2/g and (ii) with PMMA and F127 as the template in an ethanol−nitric acid solution, one can obtain 3DOM-structured γ-Al_2O_3 with the highest surface area of 145 m^2/g. The 3DOM MgO and 3DOM γ-Al_2O_3 samples possessed strong ability to uptake CO_2, while the 3DOM $Ce_{0.6}Zr_{0.4}O_2$ sample showed excellent low-temperature reducibility. We believe that the unique physicochemical properties are associated with the copresence of 3DOM architecture and mesoporous walls. Such unusual physicochemical behaviors of these porous materials make them useful in the application of heterogeneous catalysis or CO_2 adsorption.

Acknowledgment. This work was financially supported by the NSF of China (Grant No. 20473006), the SRF for ROCS (State Education Ministry of China), the PHR200907105 of the Beijing Municipal Commission of Education, and the PHR (IHLB) of Beijing Municipality.

Supporting Information Available: SEM images of PMMA microspheres; SEM and TEM images as well as SAED patterns of MgO obtained with PMMA and F127 as the template and magnesium acetate as the Mg source in 100% ethanol solution; TEM images and SAED pattern of MgO obtained with PMMA and F127 as the template and magnesium nitrate as the Mg source in a 40% ethanol solution after drying at a relative humility of 60% and then calcination at 550 °C for 5 h; SEM images, EDXS spectra, and their quantitative data of the $Ce_{0.6}Zr_{0.4}O_2$ and $Ce_{0.7}Zr_{0.3}O_2$ samples obtained with PMMA and F127 in 40% ethanol solution; and TEM images of the $Ce_{0.7}Zr_{0.3}O_2$ sample fabricated by adopting the coprecipitation method. This material is available free of charge via the Internet at http://pubs.acs.org.

IC900132K

(79) Zhou, K. B.; Wang, X.; Sun, X. M.; Peng, Q.; Li, Y. D. *J. Catal.* **2005**, *229*, 206.
(80) Ho, C.; Yu, J. C.; Kwong, T.; Mak, A. C.; Lai, S. *Chem. Mater.* **2005**, *17*, 4514.
(81) Zhang, G.; Shen, Z.; Liu, M.; Guo, C.; Sun, P.; Yuan, Z.; Li, B.; Ding, D.; Chen, T. *J. Phys. Chem. B* **2006**, *110*, 25782.
(82) (a) Yang, Z.; Zhou, K.; Liu, X.; Tian, Q.; Lu, D.; Yang, S. *Nanotechnology* **2007**, *18*, 185606. (b) Zhou, K.; Yang, Z.; Yang, S. *Chem. Mater.* **2007**, *19*, 1215. (c) Liotta, L. F.; Pantaleo, G.; Maculuso, A.; Marcì, G.; Gialanella, S.; Deganello, G. *J. Sol−Gel Sci. Technol.* **2003**, *28*, 119.
(83) Narula, C. K.; Haack, L. P.; Chun, W.; Jen, H.-W.; Graham, G. W. *J. Phys. Chem. B* **1999**, *103*, 3634.